

C-BEV: Contrastive Bird’s Eye View Training for Cross-View Image Retrieval and 3-DoF Pose Estimation

Florian Fervers¹ Sebastian Bullinger¹ Christoph Bodensteiner¹ Michael Arens¹ Rainer Stiefelhagen²

¹Fraunhofer IOSB ²Karlsruhe Institute of Technology

¹{firstname.lastname}@iosb.fraunhofer.de ²rainer.stiefelhagen@kit.edu

Abstract

To find the geolocation of a street-view image, cross-view geolocalization (CVGL) methods typically perform image retrieval on a database of georeferenced aerial images and determine the location from the visually most similar match. Recent approaches focus mainly on settings where street-view and aerial images are preselected to align w.r.t. translation or orientation, but struggle in challenging real-world scenarios where varying camera poses have to be matched to the same aerial image. We propose a novel trainable retrieval architecture that uses bird’s eye view (BEV) maps rather than vectors as embedding representation, and explicitly addresses the many-to-one ambiguity that arises in real-world scenarios. The BEV-based retrieval is trained using the same contrastive setting and loss as classical retrieval.

Our method C-BEV surpasses the state-of-the-art on the retrieval task on multiple datasets by a large margin. It is particularly effective in challenging many-to-one scenarios, e.g. increasing the top-1 recall on VIGOR’s cross-area split with unknown orientation from 31.1% to 65.0%. Although the model is supervised only through a contrastive objective applied on image pairings, it additionally learns to infer the 3-DoF camera pose on the matching aerial image, and even yields a lower mean pose error than recent methods that are explicitly trained with metric groundtruth.

1. Introduction

Visual geolocalization refers to the task of finding the geolocation of a street-view image by matching it with a database of geolocalized reference images. In the same-view setting, the query image is captured from a similar perspective as the reference images, e.g. using Google Street View [2]. Such data provide similar visual cues that facilitate the matching process, but also limit applicability to regions where they are available and sufficiently up-to-date. In the cross-view setting - also called cross-view geolocalization (CVGL) - the street-view query image is instead compared against aerial

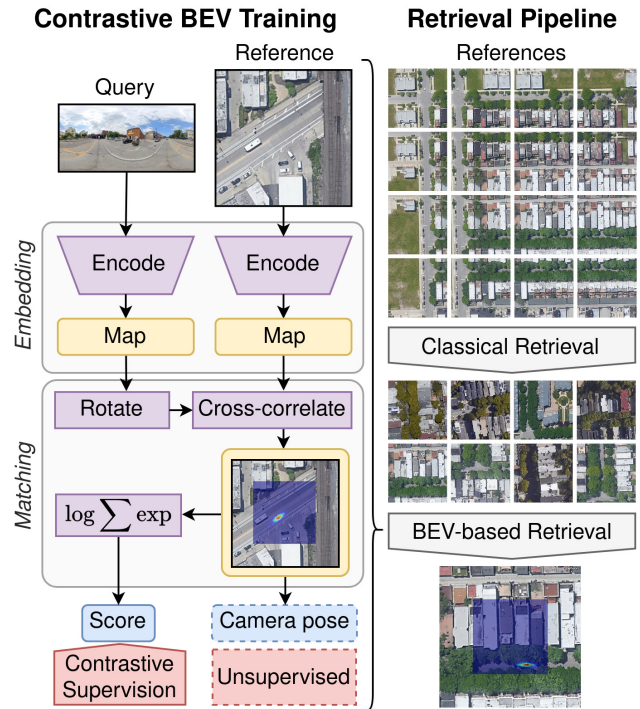


Figure 1. Overview of our novel cross-view retrieval method that uses bird’s eye view (BEV) maps as embedding representation, and finds a match by testing different 3-DoF camera poses of the street-view query on the aerial image. The model is trained using the same loss as classical retrieval architectures (e.g. CLIP [20]), and additionally learns to infer the 3-DoF camera pose on the aerial image without explicit supervision. At test time we employ a two-stage approach where candidates for a given query are determined using classical retrieval and reranked using BEV-based retrieval.

imagery as reference data. While this requires the matching to account for drastic changes in viewpoint and scale, it allows for large-scale application due to the global availability of georegistered orthophotos [1].

Current research addresses this task by tiling the aerial imagery into smaller patches and retrieving the most similar aerial image for a given street-view query image [7, 44].



(a) Similar street-views. (b) Dissimilar street-views.

Figure 2. Examples of aerial images with paired street-view images in the VIGOR [43] dataset. Different camera poses potentially lead to vastly differing street-view appearance, but have to be matched to the same aerial image. Search regions are shown in white.

The similarity is determined by training a model to map street-view and aerial images into a joint embedding space using a contrastive objective. The corresponding embedding distance reflects the likelihood that a query image is located on a reference aerial image, or a search region in the center of the image.

Embeddings have to capture relevant information from the input images while being invariant to non-distinctive image characteristics (*e.g.* lighting conditions). This presents a particular challenge in cross-view image retrieval: Different camera poses within the aerial image’s search region may lead to vastly differing street-view appearances and little to no overlap between the camera images, but have to be mapped to vector representations that align with the same aerial image (*cf.* Fig. 2).

To address this problem, we digress from the established approach of using vector embeddings, and instead utilize bird’s eye view (BEV) maps as embedding representation. A BEV map is given as a two-dimensional feature map centered on the 3-DoF camera pose. This removes the requirement for the model to predict pose-invariant embeddings, and instead shifts resolving the pose ambiguity to the matching operation between embeddings.

We test for a match between a query and reference image by considering a set of possible 3-DoF camera poses in the aerial image’s search region and aggregating the individual pose likelihoods. Each camera pose is tested by comparing the BEV map with the aerial image under the respective transformation. The entire model is end-to-end differentiable up to the retrieval scores and is trained using the same contrastive supervision as classical vector-based architectures. At test time, we first employ vector embeddings to retrieve a set of candidates and prior probabilities, and perform reranking in a second step using BEV embeddings.

Our method C-BEV achieves higher recall than previous works and is particularly effective in challenging real-world scenarios where the street-view and aerial images are not preselected to align w.r.t. translation and orientation. Additionally, the model implicitly learns to infer the metric 3-DoF pose of the street-view camera on the matching aerial image (*cf.* Fig. 6) *without seeing metric groundtruth during training*. The explicit geometric constraints in the BEV map and the matching operator represent a strong inductive bias that condition the model to solve the retrieval task by providing an estimate of the metric camera pose. The only training supervision is given via the pairwise assignment of street-view and aerial images per batch.

To summarize, our main contributions are as follows:

1. We introduce our approach C-BEV for the cross-view retrieval task that uses a novel embedding representation in the form of BEV maps and specifically addresses the many-to-one ambiguity between street-view and aerial images that arises in real-world scenarios.
2. We show that our model is able to infer the 3-DoF camera pose on the matching aerial image despite only being supervised through the retrieval objective, *i.e.* pairwise assignment of street-view and aerial images.
3. We perform extensive evaluation on several datasets to demonstrate that (a) C-BEV surpasses state-of-the-art methods on the retrieval task by a large margin and is particularly effective in more challenging scenarios, and (b) C-BEV yields 3-DoF camera poses that compare favorably even with recent methods that are explicitly supervised to perform 3-DoF camera pose estimation.

2. Related work

Cross-view geolocation refers to the problem of finding the geolocation of a street-view image by matching it against georeferenced aerial images. While early approaches use handcrafted features to match images from both domains [3, 33], to our best knowledge Lin *et al.* [13] and Workman *et al.* [37] present the first works that learn an image embedding to address the task as a retrieval problem. Workman *et al.* use a pretrained model for the street-view images and train a second model to predict aligning embeddings for the aerial images. Lin *et al.* utilize a contrastive learning objective to train a siamese model for street-view and aerial images, followed by a long thread of works that expand on this idea [6, 7, 11, 14, 27, 34, 43, 44].

Architecture Several dedicated architectures have been proposed to extract embedding vectors from the input images [27, 29, 40, 41, 45]. Many works use modules that implement a global receptive field per image, *e.g.* through spatial attention pooling [27, 41] or a multilayer perceptron (MLP) along the spatial dimensions [45]. This addresses the limited receptive field of convolutional neural networks (CNN) and helps the network reason about the spatial layout of

the scene. Recently, the transformer architecture [8, 32] has been applied to CVGL, either through a stand-alone vision transformer (ViT) [44] or in combination with convolutional neural networks (CNN) [40, 45].

Loss Several recent works employ the infoNCE [17] loss rather than a previously used (soft margin) triplet loss to model the contrastive learning objective [7, 45], which has been successfully employed in other domains such as for contrastive language-image pretraining (CLIP) [20]. Additional auxiliary loss functions have been proposed to aid the training process, such as regressing the relative rotation [6, 34] and metric translation [43] between matching aerial and ground images, or using the model as a generative adversarial network (GAN) to generate realistic aerial views from ground images [21] or ground views from aerial images [31].

Global hard sample mining As the training progresses, the model tends to classify most samples in a batch correctly and thus receives little to no supervision from the batch. To address this issue, several works employ a global hard sample mining strategy: During training, the embedding features for all images are stored in memory and updated either after every training batch [42–44], or by running inference on the entire training split every few epochs [7]. The features are used to globally mine hard samples for every training batch.

Polar transform Some works [27, 28, 31] warp the aerial image into a polar-transformed view around the position of the ground camera, such that it more closely resembles the perspective of a street-view panorama. This is only applicable on benchmarks where aerial and street-view images are preselected such that the camera’s position on the aerial image is known in advance.

State-of-the-art Deuser *et al.* [7] demonstrate that an off-the-shelf architecture without domain-specific adjustments is sufficient to outperform previous works by a large margin. They train a modern CNN [15] with a large batch size, global hard sample mining and suitable hyperparameters without using polar-transform, specialized modules or auxiliary loss functions, and achieve state-of-the-art results.

We use a retrieval architecture based on vector embeddings following their approach to yield a set of candidates for a given street-view query. In a second step, we utilize our novel BEV embeddings to rerank these candidates and achieve significantly improved recall.

Metric CVGL While cross-view image retrieval is able to account for large (*e.g.* city-scale) search regions efficiently, it provides rough geolocations only up to the size of the search region per aerial image. The metric CVGL task aims to estimate the relative 3-DoF camera pose within a matching aerial image’s search region. This problem has recently gained attention in the research community [9, 26, 38, 39, 43], with several works employing BEV maps that are matched with the aerial image over a set of discrete camera poses

[10, 24, 25, 30].

These methods require an explicit supervision of the camera pose with accurate groundtruth that is often hard to obtain and requires refinement steps (*e.g.* pseudo-labels [10] or structure-from-motion [24]) that represent restrictions on what type of data can be used. In contrast, our method learns to infer the 3-DoF camera pose despite only being supervised through a contrastive objective based on image pairings, and thus requires no metric groundtruth for the training.

3. Method

3.1. Problem formulation

We consider a dataset with n_s street-view images and n_a aerial images. Each aerial image covers a square search region in its center (*cf.* Fig. 2). If the camera location of a street-view image is within the search region, it is defined as a match for the respective aerial image. The search regions of all reference images are disjoint and cover all query locations, such that each street-view image matches with exactly one aerial image. The objective is to retrieve the matching aerial reference image for a given street-view query, and thereby provide an estimate of its geolocation.

The per-image search regions are typically chosen to cover a (*e.g.* city-scale) target region densely (*e.g.* VIGOR dataset [43]). This constitutes a many-to-one matching problem since street-view images from various camera poses have to be matched with the same aerial image (*cf.* Fig. 2). Earlier datasets represent a one-to-one mapping instead where an aerial image is preselected for each street-view query to be centered on its location (*e.g.* CVUSA [37], CVACT [14]). While street-view panoramas and aerial images in VIGOR, CVUSA and CVACT are north-aligned, we also consider the case where the street-view orientation relative to the aerial image is unknown.

Given a match between a pair of street-view and aerial images, the metric CVGL task aims to estimate the metric 3-DoF pose of the street-view image in the search region of the respective aerial image.

3.2. Overview

We present a two-stage approach to address the CVGL task (*cf.* Fig. 1):

Stage 1 Use vector embeddings to retrieve a set of possible matches from the database for a given street-view query. This allows for a cheap comparison and search in the database.

Stage 2 Use BEV embeddings to jointly (a) perform reranking on the set of candidates and (b) predict the metric 3-DoF camera pose on matching aerial images.

The first stage is responsible for ruling out easy negatives, *e.g.* when a discrimination is possible based mainly on image

semantics without considering the specific camera pose on the aerial image. It allows for a cheap query of the database especially when combined with efficient search structures. The second stage has a stronger geometric bias and explicitly considers varying camera poses to improve the recall and perform 3-DoF pose estimation (*i.e.* 2D translation and 1D rotation). Since it is computationally more expensive than the first stage and does not utilize efficient search structures, it is only applied on the set of retrieved candidates. The final score for a given reference image is computed from the vector-based prior and BEV-based update.

We separately train a model for each stage using the same contrastive image retrieval objective. At test time, the models are applied consecutively to retrieve matches for a given street-view query and predict the 3-DoF camera pose.

3.3. Stage 1: Retrieval with vector embeddings

We train a baseline model in an image retrieval setting similar to Deuser *et al.* [7] to retrieve a set of candidates from the reference database. The model learns to map both street-view and aerial images into a joint embedding space that can be used to perform nearest neighbor search at test time for a given query image.

Model We choose the ConvNeXt [15] architecture as backbone for the model. The output features are mean-pooled and L2-normalized to produce the embedding vector for a given image. We use a single model for both street-view and aerial domains which has been shown to yield better results than training separate domain-specific models [7].

Training The model is trained in a contrastive setting similar to CLIP [20]. For each training batch we sample n pairs of matching street-view and aerial images, such that each batch represents a one-to-one mapping even if the whole dataset represents a many-to-one problem. We use a symmetric cross-entropy loss that maximizes the cosine similarity of the n correct pairings, and minimizes the similarity of the $n^2 - n$ incorrect pairings in the batch.

Since the model tends to classify most samples per batch correctly as the training progresses, we employ a global hard sample mining strategy to provide stronger supervision per batch. Every e epochs, the embedding features of all training images are computed and stored in memory. For each batch, we sample hard negatives using the stored embeddings following the strategy introduced by Deuser *et al.* [7]. During the first e epochs, the haversine distance is used for determining hard negatives.

3.4. Stage 2: Retrieval with BEV embeddings

In the second stage, we utilize BEV maps rather than vectors as embedding representation that are compared to determine the matching score for a pair of images (*cf.* Fig. 1). The BEV map is given in local 3-DoF camera coordinates, and thus mitigates the challenge for the model to predict embeddings

for varying street-view camera poses that directly align with the aerial image embedding.

For each aerial image, a set of possible camera poses is sampled in a grid over the 3-DoF search volume and tested by comparing the street-view BEV map with the aerial image under the respective transformations [10, 24]. The matching score for an image pair is determined via the sum of all pose probabilities and trained end-to-end using the same loss as in vector-based retrieval. Due to the strong geometric bias in the architecture, the model learns to infer the correct 3-DoF camera pose despite receiving no direct pose supervision through the use of metric groundtruth.

Given the higher computational cost of predicting and comparing BEV maps, we apply the second stage to a set of candidates retrieved using the first stage rather than the entire dataset.

BEV encoder The embedding maps in BEV are inferred from the street-view and aerial input images. In the aerial domain, the image is already given in BEV with a known resolution and is transformed into a feature map $F_A \in \mathbb{R}^{l_A \times l_A \times c}$ with sidelength l_A and c channels using a fully-convolutional network N_A . In the street-view domain, the image is given as a panorama and transformed into a BEV map $F_B \in \mathbb{R}^{l_B \times l_B \times c}$ using a second model N_B as described below (*cf.* Fig. 3) following related works [19, 22–24].

We first extract a feature map F_P from the street-view panorama with height h and width w using a fully-convolutional network. We then transform F_P into a BEV representation F_B^{polar} in polar coordinates with w angles and d depths using an attention operation: Each cell in F_B^{polar} computes a weighted average over the corresponding column in F_P . The attention weights are predicted from F_P as a categorical distribution over d depths and normalized along the vertical axis using a softmax operation. Finally, F_B^{polar} is resampled bilinearly from polar to cartesian representation F_B . We maintain a mask with the same resolution that indicates valid cells in F_B up to a distance of $\frac{1}{2}l_B$ to the camera. Both F_A and F_B are L2-normalized globally before applying the matching operation.

BEV matching We sample a set of discrete 3-DoF camera pose hypotheses $\mathcal{H} \subset \text{SE}(2)$ in a regular grid over the search region of the aerial image with n_t translations per dimension and n_θ orientations. Each pose hypothesis $p \in \mathcal{H}$ is tested by transforming F_B into the coordinate system of F_A using p and computing the inner product between both maps, yielding an unnormalized logit for p . The results for all poses are stored in a $n_t \times n_t \times n_\theta$ score volume S . [10]

The entire volume S can be evaluated jointly and efficiently by rotating F_B by n_θ angles and computing the cross-correlation with F_A in the Fourier domain [4, 5]. We choose the size of F_B such that all unmasked cells entirely

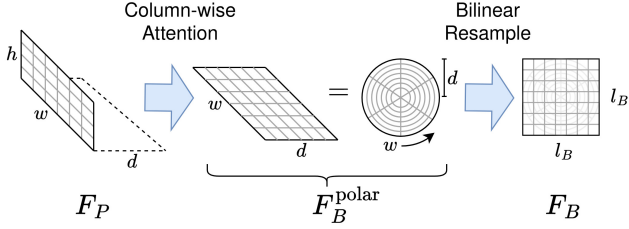


Figure 3. Transformation from street-view panorama to bird’s eye view (BEV). The feature map of the panorama image F_P with height h and width w is transformed into a polar BEV representation F_B^{polar} with w angles and d depths using an attention operation along each column. The features are then resampled bilinearly from polar to cartesian coordinates F_B .

fit onto the aerial map F_A at maximum relative offset:

$$n_t \leq l_A - l_B + 1 \quad (1)$$

Retrieval score The predicted probability for a match between a pair of images is defined as the the area under the predicted probability density function (PDF) in the aerial image’s search region. Since the PDF is represented by unnormalized logits in S , we compute the overall score $s \in \mathbb{R}$ for a match as follows:

$$s = \text{lse}(S) = \log \sum_{p \in \mathcal{H}} \exp S(h) \quad (2)$$

For a given street-view query, the probability distribution over possible aerial reference images is computed by applying a softmax operation over the respective retrieval scores.

Pose estimation The score volume S represents the likelihoods of individual camera poses in unnormalized logit representation and is transformed into a probability distribution per image using a softmax operation. The final camera pose is computed as the weighted sum over the pose hypotheses using their respective probabilities.

Training The model is trained end-to-end using the same contrastive setting as vector-based architectures. For a batch of n aerial and n street-view images, we compute the matching scores for n^2 pairs and apply the symmetric cross-entropy loss. The score volume S is not supervised directly, but only through the scalar retrieval score s .

We employ a global hard sample mining strategy by choosing the hardest neighbors for a single street-view image per batch. Since determining nearest neighbors over the entire dataset using BEV embeddings at training time is computationally infeasible, we instead utilize the learned vector embeddings from the first stage to find hard samples on the training split in the second stage. This allows for an efficient global hard sample mining and conditions the model to specialize on the failure cases of the first stage.

Testing To find matches for a given street-view query at test time, we employ learned vector embeddings to

retrieve the k highest ranked reference images. We add the BEV-based retrieval scores for all candidates onto the prior vector-based scores according to Bayes’ Theorem, and rerank the candidates w.r.t. the final scores.

4. Experiments

4.1. Data

We conduct experiments on the CVUSA [36], CVACT [14] and VIGOR [43] datasets which contain street-view panoramas with matching aerial images. We resize aerial images to shape 384×384 and panoramas to 384×768 in VIGOR and 140×768 in CVACT and CVUSA [7].

VIGOR includes translational offsets between image pairs that correspond with a search region of half the image height and width. This allows (1) applying the trained model to real-world scenarios where a region is covered densely with (overlapping) aerial images as reference database, and (2) evaluating the performance of the metric 3-DoF pose estimation. In CVUSA and CVACT, aerial images are instead always centered on a preselected street-view query.

In all three datasets, street-view panoramas and aerial images are north-aligned by default. While most recent works evaluate only in this setting, we also provide results w.r.t. unknown orientation by randomly rotating (*i.e.* horizontally shifting) the street-view panorama in the train and test splits by up to 360° . This demonstrates the feasibility of our method even in real-world scenarios where no external heading sensor is available. We decide against rotating the aerial images instead of the street-view panoramas [42], to avoid edges at the image corners or cropping (and resizing) the image to a different resolution.

The aerial images per dataset are provided with the same resolution in pixels, but cover different metric extents due to being sampled from a Mercator projection of the earth’s surface. While all aerial images in CVACT are taken at a similar latitude with roughly $6.1 \frac{\text{cm}}{\text{px}}$, images in VIGOR and CVUSA have a range of $10.1 \frac{\text{cm}}{\text{px}}$ to $11.8 \frac{\text{cm}}{\text{px}}$ and $12.7 \frac{\text{cm}}{\text{px}}$ to $27.2 \frac{\text{cm}}{\text{px}}$, respectively.

For the first stage, we rescale aerial images to 384×384 resulting in varying metric image sizes. For the BEV-based retrieval which requires consistent metric resolutions, we resize images to $16.8 \frac{\text{cm}}{\text{px}}$ in VIGOR, $19.0 \frac{\text{cm}}{\text{px}}$ in CVACT and $53.0 \frac{\text{cm}}{\text{px}}$ in CVUSA, and crop or pad the result to 384×384 pixels. More detail on the datasets is provided in the supplemental material.

4.2. Implementation details

We use the ConvNeXt-B [15] backbone as encoder for street-view and aerial images in both stages. We extract feature maps F_P and F_A at stride 8 with $l_A = 48$. We sample F_B at the same metric pixel size as F_A with a sidelength of $l_B = 48$ for CVUSA and CVACT, and $l_B = 19$ for VIGOR

Table 1. Top-k recall on the VIGOR dataset (*i.e.* with unknown translation between street-view camera and aerial image). Our baseline is the first stage of our method and trained similar to Sample4Geo [7].

	Same-area				Cross-area			
	R@1	R@5	R@10	R@1%	R@1	R@5	R@10	R@1%
Known orientation								
SAFA [27]	33.93	58.42	68.12	98.24	8.20	19.59	26.36	77.61
TransGeo [44]	61.48	87.54	91.88	99.56	18.99	38.24	46.91	88.94
SAIG [45]	65.23	88.08	-	99.68	33.05	55.94	-	94.64
Sample4Geo [7]	77.86	95.66	97.21	99.61	61.70	83.50	88.00	98.17
Baseline	78.25	95.70	97.09	99.48	61.26	82.49	86.89	98.02
C-BEV (ours)	87.49	97.65	98.26	99.48	80.01	92.02	93.33	98.02
Unknown orientation								
TransGeo [44]	47.69	79.77	86.36	99.29	5.54	14.22	19.63	66.93
Baseline	66.09	90.73	93.38	98.31	31.14	52.11	59.41	89.14
C-BEV (ours)	82.60	95.35	96.11	98.31	65.01	75.76	76.98	89.14

Table 2. Top-k recall on the CVUSA and CVACT datasets (*i.e.* with aerial images preselected to be centered on the street-view camera locations). † denotes methods that use polar transformation on the aerial input image. Our baseline is the first stage of our method and trained similar to Sample4Geo [7].

	CVUSA				CVACT-Val				CVACT-Test			
	R@1	R@5	R@10	R@1%	R@1	R@5	R@10	R@1%	R@1	R@5	R@10	R@1%
Known orientation												
SAFA † [27]	89.84	96.93	98.14	99.64	81.03	92.80	94.84	98.17	-	-	-	-
DSM [28]	91.96	97.50	98.54	99.67	82.49	92.44	93.99	97.32	-	-	-	-
LPN [35]	92.83	98.00	98.85	99.78	83.66	94.14	95.92	98.41	-	-	-	-
TransGeo [44]	94.08	98.36	99.04	99.77	84.95	94.14	95.78	98.37	-	-	-	-
GeoDTR [41]	93.76	98.47	99.22	99.85	85.43	94.81	96.11	98.26	62.96	87.35	90.70	98.61
GeoDTR † [41]	95.43	98.86	99.34	99.86	86.21	95.44	96.72	98.77	64.52	88.59	91.96	98.74
SAIG [45]	96.08	98.72	99.22	99.86	89.21	96.07	97.04	98.74	-	-	-	-
SAIG † [45]	96.34	99.10	99.50	99.86	89.06	96.11	97.08	98.89	67.49	89.39	92.30	96.80
Sample4Geo [7]	98.68	99.68	99.78	99.87	90.81	96.74	97.48	98.77	71.51	92.42	94.45	98.70
Baseline	98.17	99.72	99.80	99.85	91.42	96.69	97.47	98.80	72.35	93.10	94.92	98.77
C-BEV (ours)	98.72	99.77	99.83	99.85	91.68	96.62	97.42	98.75	75.94	93.23	94.85	98.77
Unknown orientation												
DSM [28]	78.11	89.46	92.90	98.50	72.91	85.70	88.88	95.28	-	-	-	-
Baseline	92.09	97.73	98.32	99.26	86.95	93.34	94.63	97.16	68.10	88.18	90.53	97.15
C-BEV (ours)	97.13	99.07	99.16	99.29	89.46	94.62	95.46	97.17	73.94	90.53	92.17	97.15



Figure 4. Examples of the BEV-based reranking on the VIGOR [43] dataset with unknown orientation. Each row shows a street-view query and the top-5 reference images retrieved using the first stage and ordered by decreasing matching score. A red border indicates the top-1 retrieved image after reranking in the second stage, and a red cross indicates the groundtruth position of the camera. White squares denote search regions per image.

Table 3. Ablation studies for the image retrieval on the VIGOR dataset with known orientation. Our baseline is the first stage of our method and trained similar to Sample4Geo [7].

	Same-area		Cross-area	
	R@1	R@5	R@1	R@5
Baseline	78.25	95.70	61.26	82.49
BEV resolution				
Stride 4	86.69	97.50	78.67	91.59
Stride 8	87.49	97.65	80.01	92.02
Stride 16	86.85	97.59	80.27	91.80
First stage as prior				
With	87.49	97.65	80.01	92.02
Without	84.49	95.62	76.77	90.41
Number of candidates				
$k = 10$	87.16	96.72	77.01	86.42
$k = 100$	87.49	97.65	80.01	92.02
$k = 1000$	87.54	97.78	80.31	92.83

following Eq. (1). We use 256 channels for F_P and $c = 32$ channels for F_A and F_B . The search region is sampled with $n_t = 1$ translations for CVUSA and CVACT, $n_t = 28$ translations for VIGOR and $n_\theta = 32$ angles covering 360° when evaluating with unknown orientation.

We train the first stage with a batch size of 128 for 40 epochs, update the embedding features every $e = 2$ epochs and use the AdamW [16] optimizer with learning rate 1.0×10^{-3} , cosine decay and one epoch warmup. For the second stage, we change the batch size to 18 and train for 20 epochs with learning rate 1.0×10^{-4} instead. We use label smoothing of 0.1 and a temperature of $\tau = 0.01$ in the loss function in both stages.

For data augmentation in the case of aligned orientation, we rotate both the aerial view and street view jointly by a random multiple of 90° . For unknown orientation, we rotate the street view by a random angle up to 360° and the aerial view by a multiple of 90° , separately. During the first stage, we randomly flip pairs of street-view and aerial images horizontally. At test time, we retrieve $k = 100$ reference images per query from the first stage and rerank them using the second stage.

4.3. Image retrieval

Setting We evaluate the image retrieval performance of our method C-BEV on the VIGOR (cf. Tab. 1), CVUSA and CVACT (cf. Tab. 2) datasets, each with known and unknown orientation, and report the top-k recall after the first and second stage (cf. Fig. 5).

Results Our method outperforms previous works in all evaluated many-to-one scenarios (i.e. where the relative translation or orientation between street-view and aerial images is unknown), and achieves comparable or better performance in one-to-one scenarios (i.e. where aerial images are preselected to align with street-view images w.r.t. both translation and orientation). The improvement is particularly

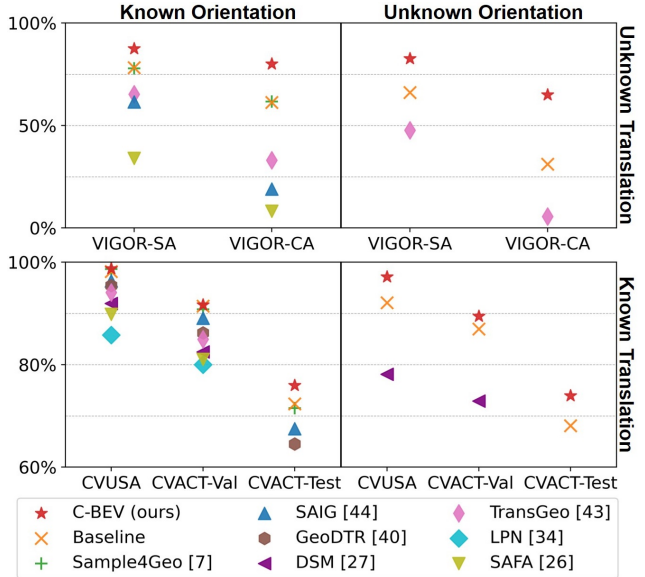


Figure 5. Top-1 recall of our retrieval method C-BEV (★) compared with previous approaches. Our work pushes the state-of-the-art by a large margin, especially in challenging real-world settings where aerial and street-view images are not preselected to align w.r.t. translation and orientation. We train our baseline (×) similar to Sample4Geo [7] (+). Most recent works consider only north-aligned images, i.e. with known orientation.

large in more challenging settings, e.g. increasing the top-1 recall on the VIGOR splits by 9.2 and 18.8 percentage points with aligned orientation and 16.5 and 33.9 points with unknown orientation. Fig. 4 shows examples of the BEV-based reranking on the VIGOR dataset.

Ablation study on BEV resolution We test for suitable resolutions of the BEV maps by encoding F_A and F_B at strides 4, 8 and 16 (i.e. $0.67 \frac{m}{px}$, $1.34 \frac{m}{px}$ and $2.68 \frac{m}{px}$) with 128, 32 and 8 channels, respectively. The resolutions are chosen such that the BEV maps have the same total size, but constitute different trade-offs between spatial resolution and representational capacity per cell. While the difference between resolutions is small, the best results are achieved at stride 8 (cf. Tab. 3).

Ablation study on first stage as soft prior To examine the impact of including the first stage’s scores as prior probabilities in the second stage’s reranking, we evaluate the retrieval performance after reranking with the BEV-based scores only (cf. Tab. 3). The recall drops slightly, indicating that the BEV-based reranking is suited most for discriminating hard samples and achieves best performance in combination with vector-based retrieval that provides a sufficient prior.

Ablation study on number of candidates Table 3 shows that reducing the number of candidates per query for the second stage from 100 to 10 results in significantly lower recall on the VIGOR cross-area split. At 1000 candidates the computation time is increased significantly, but yields

Table 4. Mean and median translation and orientation error on matching image pairs in the VIGOR dataset. *Unlike previous works, our method is trained without metric supervision and only requires pairwise assignment of images as groundtruth.

	Known orientation				Unknown orientation								
	Same-area		Cross-area		Same-area				Cross-area				
	Mean	Median	Mean	Median	Mean	Median	Mean	Median	Mean	Median			
Supervised													
CVR [43]	8.99m	7.81m	8.89m	7.73m	-	-	-	-	-	-	-	-	-
MCC [39]	6.94m	3.64m	9.05m	5.14m	9.87m	56.86°	6.25m	16.02°	12.66m	72.13°	9.55m	29.97°	
SliceMatch [12]	5.18m	2.58m	5.53m	2.55m	6.49m	25.46°	3.13m	4.71°	7.22m	25.97°	3.31m	4.51°	
GGCVT [30]	4.12m	1.34m	5.16m	1.40m	-	-	-	-	-	-	-	-	-
Unsupervised*													
C-BEV (ours)	3.52m	2.58m	3.97m	2.86m	3.85m	5.55°	2.81m	2.16°	4.78m	7.90°	3.48m	2.52°	

only small improvement. We choose $k = 100$ candidates as a trade-off between runtime and recall.

Runtime and scalability We evaluate the runtime of the retrieval on the VIGOR dataset using an Nvidia H100. Our implementation tests multiple reference images per query in parallel. The computation of embedding maps F_A and F_B requires about 1.3ms and 4.6ms, respectively. The matching operation requires about 0.1ms to 0.3ms per candidate, dependent on the choice of n_θ up to 32.

We rerank 100 candidates per query image in the VIGOR dataset, *i.e.* about 0.1% of the possible reference images each covering a search region of about $35\text{m} \times 35\text{m}$. Given an area that is densely covered with aerial images in a similar setup, the reranking incurs an additional cost of $(\frac{1000\text{m}}{35\text{m}})^2 \cdot 0.1\% \approx 1$ matching operation per square kilometer. Without precomputed BEV embeddings, this corresponds to roughly 1.4ms to 1.6ms per square kilometer, and about 4 hours for the land area of the United States.

4.4. Pose estimation

Setting We evaluate the pose estimation performance of C-BEV on matching image pairs in the VIGOR dataset (*cf.* Tab. 4) with known and unknown orientation and report the mean and median translation and orientation error.

Results Our method achieves a better mean pose error than recent pose estimation methods on VIGOR in all settings despite training without any metric groundtruth. Fig. 6 shows examples of the predicted probability distributions over possible camera locations in the search region.

The latest supervised work GGCVT [30] achieves a smaller median position error for the case of aligned orientation, but larger mean error than our method. The gap between mean and median metrics indicates that C-BEV is better at providing a rough camera pose estimate, but does not achieve the same fine accuracy as GGCVT.

Ablation study on search region boundary To further examine the model’s ability to infer accurate camera locations without explicit supervision, we consider the case of street-view images being located close to the search region boundary. Here, the loss might provide direct metric supervision by penalizing small offsets of the predicted camera



Figure 6. Examples of probability distributions over camera locations predicted by our method. The model learns to infer the camera pose despite not receiving metric supervision during training. Search regions are larger than half the image diameter due to the cropping of images described in Sec. 4.1.

location across the search region boundary onto a negative reference image. To test this hypothesis, we train a model by excluding negative reference images per batch that are located closer than 50m to a street-view query. The resulting model yields only marginally worse pose predictions, which suggests that boundary cases are not the primary cause of the model’s ability to infer camera locations without direct supervision.

5. Conclusion

We introduce our method C-BEV for the cross-view geo-localization task. Our approach uses a novel embedding representation in the form of bird’s eye view maps, and specifically addresses the many-to-one ambiguity that arises when varying street-view camera poses with vastly differing visual appearances have to be matched to the same aerial image.

C-BEV surpasses the state-of-the-art on the cross-view image retrieval task by a large margin, especially in challenging real-world settings. Even though we use only a contrastive objective applied on image pairings as supervision during training, our model learns to infer the 3-DoF camera pose on the matching aerial image, and even yields a better mean pose error than recent methods explicitly trained with metric groundtruth.

References

- [1] Google maps. <https://www.google.com/maps>, . 1
- [2] Google street view. <https://developers.google.com/maps/documentation/streetview/intro>, . 1
- [3] Mayank Bansal, Harpreet S Sawhney, Hui Cheng, and Kostas Daniilidis. Geo-localization of street views with aerial image databases. In *Proceedings of the 19th ACM international conference on Multimedia*, pages 1125–1128, 2011. 2
- [4] Dan Barnes, Rob Weston, and Ingmar Posner. Masking by moving: Learning distraction-free radar odometry from pose information. *arXiv preprint arXiv:1909.03752*, 2019. 4
- [5] Ioan Andrei Barsan, Shenlong Wang, Andrei Pokrovsky, and Raquel Urtasun. Learning to localize using a lidar intensity map. *arXiv preprint arXiv:2012.10902*, 2020. 4
- [6] Sudong Cai, Yulan Guo, Salman Khan, Jiwei Hu, and Gongjian Wen. Ground-to-aerial image geo-localization with a hard exemplar reweighting triplet loss. In *Proceedings of the IEEE/CVF International Conference on Computer Vision*, pages 8391–8400, 2019. 2, 3
- [7] Fabian Deuser, Konrad Habel, and Norbert Oswald. Sample4geo: Hard negative sampling for cross-view geo-localisation. In *Proceedings of the IEEE/CVF International Conference on Computer Vision (ICCV)*, pages 16847–16856, 2023. 1, 2, 3, 4, 5, 6, 7, 11, 13
- [8] Alexey Dosovitskiy, Lucas Beyer, Alexander Kolesnikov, Dirk Weissenborn, Xiaohua Zhai, Thomas Unterthiner, Mostafa Dehghani, Matthias Minderer, Georg Heigold, Sylvain Gelly, et al. An image is worth 16x16 words: Transformers for image recognition at scale. *arXiv preprint arXiv:2010.11929*, 2020. 3
- [9] Florian Fervers, Sebastian Bullinger, Christoph Bodensteiner, Michael Arens, and Rainer Stiefelhagen. Continuous self-localization on aerial images using visual and lidar sensors. In *2022 IEEE/RSJ International Conference on Intelligent Robots and Systems (IROS)*, pages 7028–7035. IEEE, 2022. 3
- [10] Florian Fervers, Sebastian Bullinger, Christoph Bodensteiner, Michael Arens, and Rainer Stiefelhagen. Uncertainty-aware vision-based metric cross-view geolocalization. In *Proceedings of the IEEE/CVF Conference on Computer Vision and Pattern Recognition*, pages 21621–21631, 2023. 3, 4
- [11] Sixing Hu, Mengdan Feng, Rang MH Nguyen, and Gim Hee Lee. Cvm-net: Cross-view matching network for image-based ground-to-aerial geo-localization. In *Proceedings of the IEEE Conference on Computer Vision and Pattern Recognition*, pages 7258–7267, 2018. 2
- [12] Ted Lentsch, Zimin Xia, Holger Caesar, and Julian FP Kooij. Slicematch: Geometry-guided aggregation for cross-view pose estimation. In *Proceedings of the IEEE/CVF Conference on Computer Vision and Pattern Recognition*, pages 17225–17234, 2023. 8
- [13] Tsung-Yi Lin, Yin Cui, Serge Belongie, and James Hays. Learning deep representations for ground-to-aerial geolocalization. In *Proceedings of the IEEE conference on computer vision and pattern recognition*, pages 5007–5015, 2015. 2
- [14] Liu Liu and Hongdong Li. Lending orientation to neural networks for cross-view geo-localization. In *Proceedings of the IEEE/CVF conference on computer vision and pattern recognition*, pages 5624–5633, 2019. 2, 3, 5, 11, 12
- [15] Zhuang Liu, Hanzi Mao, Chao-Yuan Wu, Christoph Feichtenhofer, Trevor Darrell, and Saining Xie. A convnet for the 2020s. In *Proceedings of the IEEE/CVF conference on computer vision and pattern recognition*, pages 11976–11986, 2022. 3, 4, 5
- [16] Ilya Loshchilov and Frank Hutter. Decoupled weight decay regularization. *arXiv preprint arXiv:1711.05101*, 2017. 7
- [17] Aaron van den Oord, Yazhe Li, and Oriol Vinyals. Representation learning with contrastive predictive coding. *arXiv preprint arXiv:1807.03748*, 2018. 3
- [18] OpenStreetMap contributors. Planet dump retrieved from <https://planet.osm.org>. <https://www.openstreetmap.org>, 2017. 12
- [19] Jonah Philion and Sanja Fidler. Lift, splat, shoot: Encoding images from arbitrary camera rigs by implicitly unprojecting to 3d. In *Computer Vision—ECCV 2020: 16th European Conference, Glasgow, UK, August 23–28, 2020, Proceedings, Part XIV 16*, pages 194–210. Springer, 2020. 4
- [20] Alec Radford, Jong Wook Kim, Chris Hallacy, Aditya Ramesh, Gabriel Goh, Sandhini Agarwal, Girish Sastry, Amanda Askell, Pamela Mishkin, Jack Clark, et al. Learning transferable visual models from natural language supervision. In *International conference on machine learning*, pages 8748–8763. PMLR, 2021. 1, 3, 4
- [21] Krishna Regmi and Mubarak Shah. Bridging the domain gap for ground-to-aerial image matching. In *Proceedings of the IEEE/CVF International Conference on Computer Vision*, pages 470–479, 2019. 3
- [22] Thomas Roddick and Roberto Cipolla. Predicting semantic map representations from images using pyramid occupancy networks. In *Proceedings of the IEEE/CVF Conference on Computer Vision and Pattern Recognition*, pages 11138–11147, 2020. 4
- [23] Avishkar Saha, Oscar Mendez, Chris Russell, and Richard Bowden. Translating images into maps. In *2022 International conference on robotics and automation (ICRA)*, pages 9200–9206. IEEE, 2022.
- [24] Paul-Edouard Sarlin, Daniel DeTone, Tsun-Yi Yang, Armen Avetisyan, Julian Straub, Tomasz Malisiewicz, Samuel Rota Bulò, Richard Newcombe, Peter Kotschieder, and Vasileios Balntas. Orienternet: Visual localization in 2d public maps with neural matching. In *Proceedings of the IEEE/CVF Conference on Computer Vision and Pattern Recognition*, pages 21632–21642, 2023. 3, 4
- [25] Paul-Edouard Sarlin, Eduard Trulls, Marc Pollefeys, Jan Hosang, and Simon Lymen. Snap: Self-supervised neural maps for visual positioning and semantic understanding. *arXiv preprint arXiv:2306.05407*, 2023. 3
- [26] Yujiao Shi and Hongdong Li. Beyond cross-view image retrieval: Highly accurate vehicle localization using satellite image. In *Proceedings of the IEEE/CVF Conference on Computer Vision and Pattern Recognition*, pages 17010–17020, 2022. 3
- [27] Yujiao Shi, Liu Liu, Xin Yu, and Hongdong Li. Spatial-aware feature aggregation for image based cross-view geo-

- localization. *Advances in Neural Information Processing Systems*, 32, 2019. 2, 3, 6
- [28] Yujiao Shi, Xin Yu, Dylan Campbell, and Hongdong Li. Where am i looking at? joint location and orientation estimation by cross-view matching. In *Proceedings of the IEEE/CVF Conference on Computer Vision and Pattern Recognition*, pages 4064–4072, 2020. 3, 6
- [29] Yujiao Shi, Xin Yu, Liu Liu, Tong Zhang, and Hongdong Li. Optimal feature transport for cross-view image geo-localization. In *Proceedings of the AAAI Conference on Artificial Intelligence*, pages 11990–11997, 2020. 2
- [30] Yujiao Shi, Fei Wu, Akhil Perincherry, Ankit Vora, and Hongdong Li. Boosting 3-dof ground-to-satellite camera localization accuracy via geometry-guided cross-view transformer. In *Proceedings of the IEEE/CVF International Conference on Computer Vision*, pages 21516–21526, 2023. 3, 8
- [31] Aysim Toker, Qunjie Zhou, Maxim Maximov, and Laura Leal-Taixé. Coming down to earth: Satellite-to-street view synthesis for geo-localization. In *Proceedings of the IEEE/CVF Conference on Computer Vision and Pattern Recognition*, pages 6488–6497, 2021. 3
- [32] Ashish Vaswani, Noam Shazeer, Niki Parmar, Jakob Uszkoreit, Llion Jones, Aidan N Gomez, Łukasz Kaiser, and Illia Polosukhin. Attention is all you need. *Advances in neural information processing systems*, 30, 2017. 3
- [33] Anirudh Viswanathan, Bernardo R Pires, and Daniel Huber. Vision based robot localization by ground to satellite matching in gps-denied situations. In *2014 IEEE/RSJ International Conference on Intelligent Robots and Systems*, pages 192–198. IEEE, 2014. 2
- [34] Nam N Vo and James Hays. Localizing and orienting street views using overhead imagery. In *Computer Vision—ECCV 2016: 14th European Conference, Amsterdam, The Netherlands, October 11–14, 2016, Proceedings, Part I 14*, pages 494–509. Springer, 2016. 2, 3
- [35] Tingyu Wang, Zhedong Zheng, Chenggang Yan, Jiyong Zhang, Yaoqi Sun, Bolun Zheng, and Yi Yang. Each part matters: Local patterns facilitate cross-view geo-localization. *IEEE Transactions on Circuits and Systems for Video Technology*, 32(2):867–879, 2021. 6
- [36] Scott Workman, Richard Souvenir, and Nathan Jacobs. Wide-area image geolocalization with aerial reference imagery. In *International Conference on Computer Vision*, 2015. 5
- [37] Scott Workman, Richard Souvenir, and Nathan Jacobs. Wide-area image geolocalization with aerial reference imagery. In *Proceedings of the IEEE International Conference on Computer Vision*, pages 3961–3969, 2015. 2, 3, 11, 12
- [38] Zimin Xia, Olaf Booij, Marco Manfredi, and Julian FP Kooij. Cross-view matching for vehicle localization by learning geographically local representations. *IEEE Robotics and Automation Letters*, 6(3):5921–5928, 2021. 3
- [39] Zimin Xia, Olaf Booij, Marco Manfredi, and Julian FP Kooij. Visual cross-view metric localization with dense uncertainty estimates. In *European Conference on Computer Vision*, pages 90–106. Springer, 2022. 3, 8
- [40] Hongji Yang, Xiufan Lu, and Yingying Zhu. Cross-view geo-localization with layer-to-layer transformer. *Advances in Neural Information Processing Systems*, 34:29009–29020, 2021. 2, 3, 11, 13
- [41] Xiaohan Zhang, Xingyu Li, Waqas Sultani, Yi Zhou, and Safwan Wshah. Cross-view geo-localization via learning disentangled geometric layout correspondence. In *Proceedings of the AAAI Conference on Artificial Intelligence*, pages 3480–3488, 2023. 2, 6, 13
- [42] Sijie Zhu, Taojiannan Yang, and Chen Chen. Revisiting street-to-aerial view image geo-localization and orientation estimation. In *Proceedings of the IEEE/CVF Winter Conference on Applications of Computer Vision*, pages 756–765, 2021. 3, 5
- [43] Sijie Zhu, Taojiannan Yang, and Chen Chen. Vigor: Cross-view image geo-localization beyond one-to-one retrieval. In *Proceedings of the IEEE/CVF Conference on Computer Vision and Pattern Recognition*, pages 3640–3649, 2021. 2, 3, 5, 6, 8, 11, 12
- [44] Sijie Zhu, Mubarak Shah, and Chen Chen. Transgeo: Transformer is all you need for cross-view image geo-localization. In *Proceedings of the IEEE/CVF Conference on Computer Vision and Pattern Recognition*, pages 1162–1171, 2022. 1, 2, 3, 6
- [45] Yingying Zhu, Hongji Yang, Yuxin Lu, and Qiang Huang. Simple, effective and general: A new backbone for cross-view image geo-localization. *arXiv preprint arXiv:2302.01572*, 2023. 2, 3, 6

Appendix

A. Overview of datasets

Fig. 7 gives an overview of the datasets used for evaluation in this paper. In VIGOR, aerial images cover several regions densely (*cf.* Sec. 3.1), and up to two street-view queries are chosen in the search region of each reference image. In CVUSA and CVACT, aerial images are preselected to align with a set of street-view images.

All aerial images per dataset are sampled with the same size in pixels from a Mercator projection of the earth’s surface. As a consequence, the size in meters (*cf.* Tab. 5) changes with the image’s latitude (*i.e.* distance north or south of the equator).

B. Effect of metric pixel size

Setting We report results for cross-dataset image retrieval (*cf.* Tab. 6) where the models trained on CVUSA and CVACT are also tested on each other’s validation splits as proposed by Yang *et al.* [40], denoted as CVUSA → CVACT and CVACT → CVUSA.

Effect of metric pixel size For our baseline using vector embeddings, we rescale all aerial images with the same factor per dataset to 384×384 pixels following related works and achieve similar results as the current state-of-the-art method Sample4Geo [7]. Resizing the images to a consistent pixel size of $19.0 \frac{\text{cm}}{\text{px}}$ already improves the baseline results significantly, even though a large portion of the images in CVUSA are cropped as a consequence. This indicates that the model does not generalize well to aerial images with unseen scale. However, such a capability is not required in the context of cross-view geolocalization: Aerial images are always georeferenced and their scale is known, such that they can be resized as required.

Of the datasets used in this work (*cf.* Tab. 6), we observe the impact of resizing aerial images to consistent metric pixel sizes mainly in the cross-dataset setting. *E.g.* in CVACT → CVUSA, models are trained on images with side-length 73m and tested on 95m to 204m. While the CVUSA dataset also contains images with varying pixel sizes, this range is the same in both train and test splits, such that all scales are also seen during training. In this case, resizing images to the same metric pixel size (with corresponding cropping or padding to 384×384 pixels) degrades the performance, potentially due to the loss of information incurred from cropping or using coarser pixel resolutions.

Our evaluation demonstrates that training and testing on the same range of metric pixel sizes is preferred. We thus report our main results in Sec. 4 on splits where the range of pixel sizes of testing images is contained in or close to the range of the training images.

Table 5. Sidelength (in meters) of aerial images in datasets used in this work. Each row corresponds to a different train-test split.

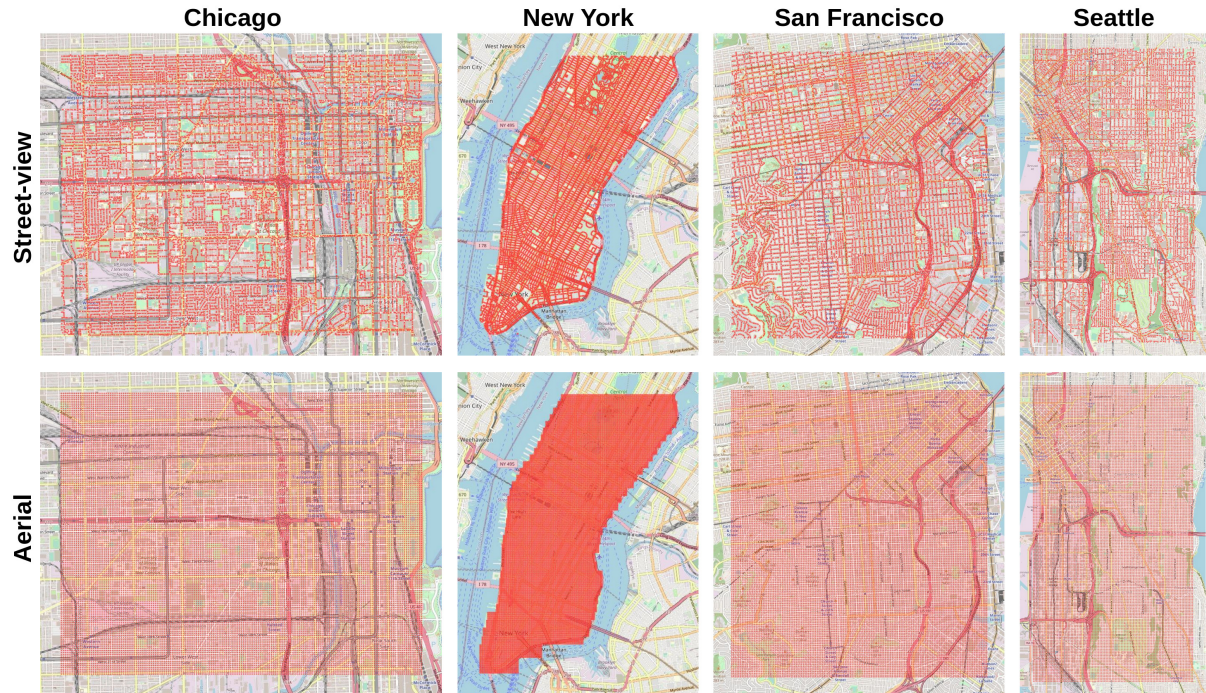
	Training images		Testing images	
	Min.	Max.	Min.	Max.
VIGOR same-area [43]	64.3	75.3	64.3	75.3
VIGOR cross-area [43]	64.3	72.3	71.0	75.3
CVUSA [37]	95.1	203.7	95.2	203.5
CVACT-Val [14]	72.8	72.8	72.8	72.9
CVACT-Test [14]	72.8	72.8	72.8	72.9
CVUSA → CVACT	95.1	203.7	72.8	72.9
CVACT → CVUSA	72.8	72.8	95.2	203.5

Results of our method We report results of C-BEV in the cross-dataset setting with images resized to $19.0 \frac{\text{cm}}{\text{px}}$ (and cropped to 384×384 pixels) as it requires consistent pixel sizes. Since related works evaluate with the original metric sizes, we train a model similar to the best previous work Sample4Geo [7] using resized images as our baseline.

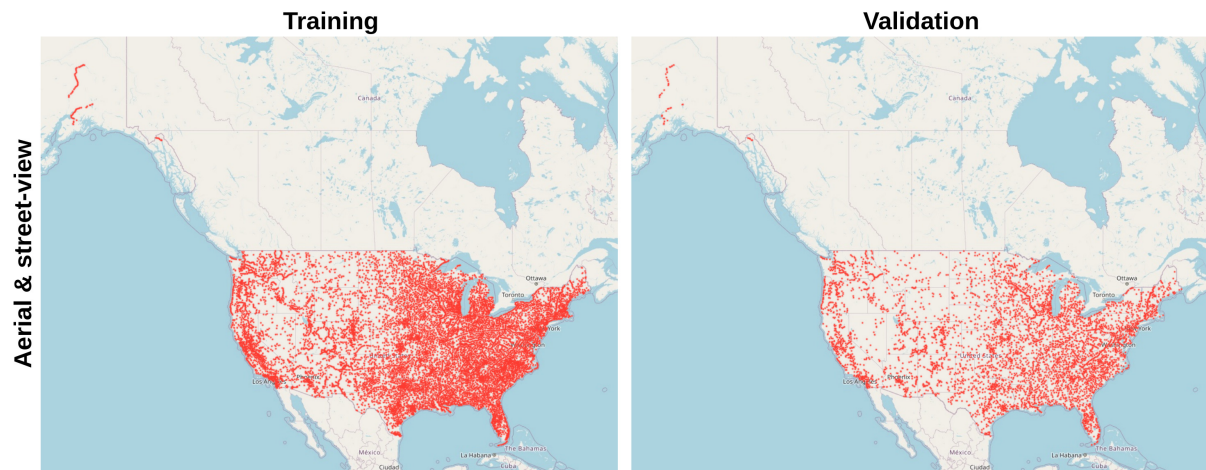
Our method improves the results significantly, especially in challenging settings where current state-of-the-art approaches do not perform well. In the case of unknown orientation, the top-1 recall is improved by 22.7 and 9.2 percentage points over the baseline.

C. Effect of search region boundary

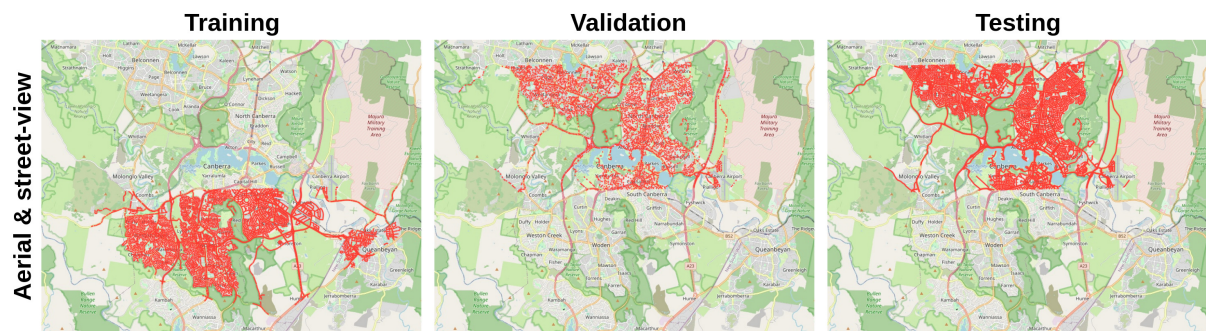
We evaluate the 3-DoF pose estimation performance of our method on the VIGOR dataset with a minimum distance between street-view images and negative aerial reference images per batch to examine the impact of query images being located close to the search region boundary as discussed in Sec. 4.4. Table 7 shows that the recall drops only slightly when including an offset of 50m, indicating that search region boundaries are not primarily responsible for the ability of the model to infer the 3-DoF camera pose without explicit supervision.



(a) Images in VIGOR [43] are captured in four different cities in the United States. Every dot represents the location of an image. Aerial images cover a region in a regular grid while street-view images are sampled at random locations.



(b) Images in CVUSA [37] are captured in the United States. Every dot represents a pair of aligned street-view and aerial images.



(c) Images in CVACT [14] are captured in the Australian Capital Territory. Every dot represents a pair of aligned street-view and aerial images.

Figure 7. Overview of image locations in datasets used in this work. Map data from [OpenStreetMap](#) [18].

Table 6. Top-k recall in a cross-dataset setting as proposed by Yang *et al.* [40]: Models are trained on the CVUSA and CVACT training splits and tested on each other’s validation splits. Our baseline is the first stage of our method and trained similar to Sample4Geo [7]. † denotes methods that use polar transformation on the aerial input image. * indicates that images in CVUSA and CVACT are resized to the same metric size with $19.0 \frac{\text{cm}}{\text{px}}$.

	CVUSA → CVACT				CVACT → CVUSA			
	R@1	R@5	R@10	R@1%	R@1	R@5	R@10	R@1%
Known orientation								
L2LTR† [40]	47.55	70.58	77.39	91.39	33.00	51.87	60.63	84.79
GeoDTR† [41]	53.16	75.62	81.90	93.80	44.07	64.66	72.08	90.09
Sample4Geo [7]	56.62	77.79	87.02	94.69	44.95	64.36	72.10	90.65
Baseline	58.73	82.35	87.65	96.41	42.72	64.99	72.97	92.45
Baseline*	85.02	95.50	96.68	98.47	64.77	79.91	84.85	96.09
C-BEV* (ours)	88.07	96.15	97.07	98.46	70.01	83.57	87.82	96.25
Unknown orientation								
Baseline	25.87	45.99	54.66	79.11	12.70	24.30	30.55	55.14
Baseline*	55.32	76.18	81.70	92.91	35.49	49.47	55.39	74.58
C-BEV* (ours)	78.06	88.63	90.30	93.37	44.71	56.80	61.89	75.37

Table 7. Mean and median translation and orientation error of our method C-BEV on matching image pairs in the VIGOR dataset. We add a minimum distance between street-view queries and negative reference images per batch in the data sampler during training.

Min. distance	Known orientation				Unknown orientation							
	Same-area		Cross-area		Same-area				Cross-area			
	Mean	Median	Mean	Median	Mean	Median	Mean	Median	Mean	Median	Mean	Median
0m	3.52m	2.58m	3.97m	2.86m	3.87m	5.56°	2.81m	2.16°	4.78m	7.90°	3.48m	2.52°
50m	3.53m	2.70m	4.21m	3.31m	3.82m	5.64°	2.81m	2.20°	5.04m	8.24°	3.70m	2.66°